Dynamics of scattering in undulatory active collisions

Jennifer M. Rieser,[1,*] Perrin E. Schiebel,[1] Arman Pazouki,[2] Feifei Qian,[3,†] Zachary Goddard,[4] Kurt Wiesenfeld,[1] Andrew Zangwill,[1] Dan Negrut,[5] and Daniel I. Goldman[1,‡]

[1]*School of Physics, Georgia Institute of Technology, Atlanta, GA 30332, USA*
[2]*Department of Mechanical Engineering, California State University, Los Angeles, CA 90032, USA*
[3]*School of Electrical and Computer Engineering, Georgia Institute of Technology, Atlanta, GA 30332, USA*
[4]*School of Mechanical Engineering, Georgia Institute of Technology, Atlanta, GA 30332, USA*
[5]*Department of Mechanical Engineering, University of Wisconsin—Madison, Madison, WI 53706, USA*

(Received 15 March 2018; published 8 February 2019)

Natural and artificial self-propelled systems must manage environmental interactions during movement. In complex environments, these interactions include *active collisions*, in which propulsive forces create persistent contacts with heterogeneities. Due to the driven and dissipative nature of these systems, such collisions are fundamentally different from those typically studied in classical physics. Here we experimentally and numerically study the effects of active collisions on a laterally undulating sensory-deprived robophysical model, whose dynamics are relevant to self-propelled systems across length scales and environments. Interactions with a single rigid post scatter the robot, and this deflection is dominated by head-post contact. These results motivate a model which reduces the snake to a circular particle with two key features: The collision dynamics are set by internal driving subject to the geometric constraints of the post, and the particle has an effective length equal to the wavelength of the snake. Interactions with a single row of evenly spaced posts (with interpost spacing d) produce distributions reminiscent of far-field diffraction patterns: As d decreases, distinct secondary peaks emerge as large deflections become more likely. Surprisingly, we find that the presence of multiple posts does not change the nature of individual collisions; instead, multimodal scattering patterns arise from multiple posts altering the likelihood of individual collisions to occur. As d decreases, collisions near the leading edges of the posts become more probable, and we find that these interactions are associated with larger deflections. Our results, which highlight the surprising dynamics that can occur during active collisions of self-propelled systems, can inform control principles for locomotors in complex terrain and facilitate design of task-capable active matter.

DOI: 10.1103/PhysRevE.99.022606

I. INTRODUCTION

Biological and artificial systems must manage mechanical interactions with the environment to generate and sustain movement. These interactions come in myriad forms, from repeated impacts with rigid ground [1] to managing and manipulating flowable substrates like granular media [2] and fluids [3]. We refer to the interactions between self-propelled systems and heterogeneities in the surrounding environment as *active collisions*. As noted in Ref. [4], conservation of momentum does not apply to collisions in these dissipative and driven systems. As a result, the framework of classical scattering theory is unable to capture the diverse and rich behavior arising from active collisions.

Whether the interactions are among like individuals or between an individual and a heterogeneity, many share a common feature: The driving allows for *persistent* interactions. These interactions are an important factor in many systems spanning a wide range of length scales, from the aggregation of bacteria near surfaces to form biofilms [5], the self-assembly and disassembly of colloidal clusters [6], and the scattering of spermatozoa and *Chlamydomonas* from surfaces [7] to locomotion of animals and robots.

Such interactions often hinder movement. For example, *Escherichia coli* experience a speed reduction near walls [8], self-propelled rods are geometrically captured by cylindrical obstacles [9], and collections of self propelled particles can become jammed in disordered landscapes [10]. In robotic systems, motion planning algorithms often focus on collision avoidance rather than resolution [11]. However, if properly utilized, these interactions can benefit locomotion. For example, rapidly running cockroaches use exoskeletal interactions to maneuver through grass [12] and clutter [13]; sand-specialist snakes experience environmentally induced passive body deformations that enable obstacle negotiation and rapid transit through complex terrain [14]; generalist snakes use body parts to propel from bark and rubble [15]; and *Caenorhabditis elegans* use environmental structures to enhance propulsion [16]. In robotics, properly tuned dynamical systems can take advantage of periodic mechanical interactions to produce sustained movement [13,17–19] and properly timed tail-ground interactions improve performance

*jennifer.rieser@physics.gatech.edu
†Present address: Department of Electrical and Systems Engineering, University of Pennsylvania, Philadelphia, PA 19104, USA.
‡daniel.goldman@physics.gatech.edu

on yielding substrates [20] and can reduce the effects of collisions [21].

In active systems, interactions and collisions with the environment are persistent, and only when the velocity is directed away from the obstacle or boundary is detachment possible (provided the individual can overcome any other pinning forces and torques). In the microscopic realm, the direction of driving is typically modeled stochastically (arising from Brownian motion) and can include a rotational diffusion term [22]. The strength of the driving and the size of the orientational variations dictate the duration of the interaction as well as the outcome. While the mechanisms by which the orientation can change are different in macroscopic systems, typically either induced by environmental interactions or inherent in the self-propulsion, the ability to reorient remains important for breaking contact with and maneuvering through obstacles. A recent study of environmentally induced passive reorientation found that a robophysical cockroach was more successful in traversing narrow openings when biologically inspired body vibrations were added [23].

We study a system in which the orientation is inherent in the self-propulsion of a long slender locomotor that uses *undulatory propulsion*, in which body bends originate at the head and are subsequently passed down the body to generate movement [24]. This mode of locomotion is observed over a broad range of length scales and produces effective movement in a wide range of environments, from swimming in fluids (e.g., spermatozoa [25], nematodes [26], and aquatic vertebrates [27,28]) to slithering on and within granular materials (e.g., nematodes [29], lizards [30], and snakes [31]) to traversing complex environments (e.g., nematodes [16,32,33] and snakes [15,34]). In particular, we will focus on *lateral undulation*, in which body bends only occur in the horizontal plane. Despite this restriction, this form of propulsion is still quite general, being the only mode of locomotion shared by all limbless terrestrial vertebrates [35]).

Here we take a robophysics [36] approach, building on our previous work [37] to explore the nature of the interactions underlying active collisions occurring during undulatory self-propulsion in dissipative environments. Details of our experimental and numerical systems are described in Sec. II. Section III A examines interactions with a single obstacle and shows that collisions rotate the robot's trajectory; Sec. III B demonstrates that this rotation is dominated by head-obstacle collisions. These results motivate the model presented in Sec. III C, which recovers scattering dynamics by reducing the robot to a circular particle and prescribing new collision rules. Section III D uses insights from the model to define a natural collision state space. Section III E extends our investigation to interactions with multiple posts. Surprisingly, scattering patterns produced by a row of evenly spaced posts are reminiscent of far-field diffraction. Section III F shows that multiple-post interactions are still dominated by a single head-obstacle interaction, and Sec. III G shows that collision states are unaltered by the presence of multiple posts, revealing that scattering patterns are generated by altering the distribution of collision states. We close in Sec. IV with a summary of our results as well as a discussion of our work and future studies in the context of driven systems.

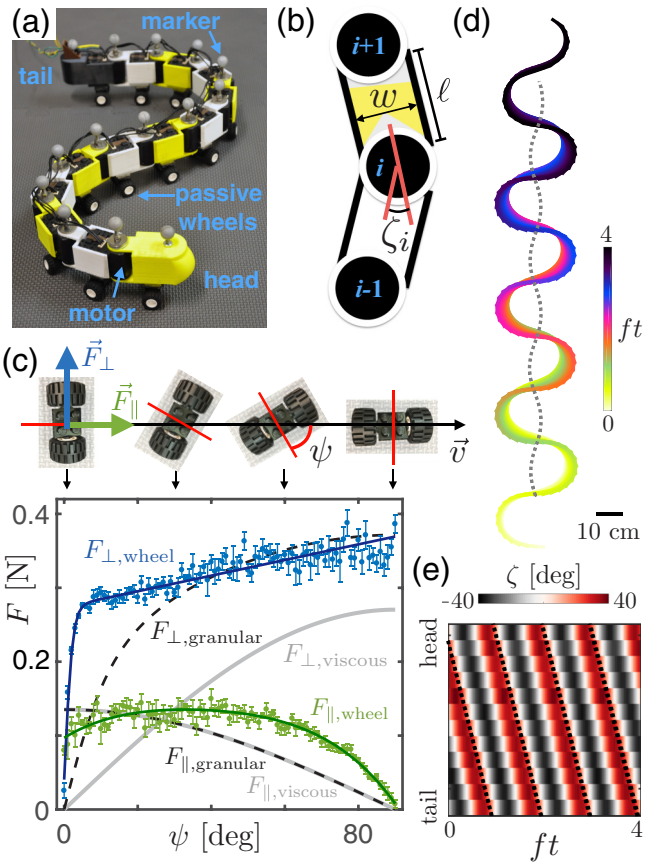

FIG. 1. Robophysical snake movement. (a) Robotic snake constructed from servo motors and three-dimensional-printed brackets. Passive wheels affixed to the bottom of each segment enabled the robot to translate, and markers atop each motor were used to track segment positions over time. (b) A schematic of three adjacent servo motors (black circles). The angular position of each motor, ζ_i, was driven as a function of time. (c) Experimentally measured steady-state wheel forces along (green) and perpendicular to (blue) the rolling direction. Error bars indicate variation over five trials and curves show fits to data. For comparison, drag forces are shown for 300-μm glass particles (dashed black lines) and for viscous fluid (light gray lines). Forces are scaled so that all $\vec{F}_\parallel$ curves have the same maximum value. (d) Robot configurations while moving in a post-free environment. The dashed gray curve shows the corresponding center-of-geometry trajectory. (e) A space-time plot shows experimentally measured ζ_i for the trajectory shown in (d). Dashed lines highlight the same band of constant positive ζ in each undulation cycle.

II. METHODS

To gain physical insight into active collisions during undulatory self-propulsion, we adopted a robophysical approach and created a laterally undulating sensory-deprived robotic snake [Fig. 1(a)]. Thirteen segments were connected together by $N = 12$ servo motors, each of which was oriented so that actuation controlled the angular position within the horizontal plane. Body bends that originated at the head and subsequently propagated down the body were produced by commanding the angular position, ζ_i, of each motor, i, to vary sinusoidally in time: $\zeta_i(t) = \zeta_{\max} \sin(2\pi i/N - 2\pi ft)$,

creating a *serpenoid* curve [38] [see Fig. 1(b)]. Here $f = 0.15$ Hz is the frequency of undulation, and $\zeta_{\max} = 40^\circ$ is the angular amplitude.

Translational motion of the robot was achieved from the motor-angle actuation through a frictional anisotropy, created by affixing a pair of passive wheels (connected by an axle) to the bottom of each robot segment [39], see Fig. 1(a). To estimate the ground reaction forces for a single robot segment, steady-state drag forces were measured in separate experiments (see Ref. [40]) as a single wheel pair with normal force equal to the weight of a robot segment was translated across the experimental substrate at constant speed [see Fig. 1(c)]. For comparison, drag force relations are shown for other dissipative environments: a submerged rod translated through granular material [31] and a slender rod moving through a viscous fluid [41].

A typical low-slip trajectory of the robot resulting from the serpenoid motion and the wheel-ground interaction is shown in Fig. 1(d). Experimentally measured ζ_i throughout this trajectory (determined from the segment positions) are shown in the space-time plot in Fig. 1(e). The head-to-tail wave progression is confirmed by the diagonal stripes, and the consistency of these stripes throughout four undulations shows that the robot motors reliably followed the prescribed motion.

Heterogeneous environments were created by anchoring either one or five rigid, vertical, force-sensitive cylindrical posts to an otherwise-homogeneous substrate [see Fig. 2(a)]. Example trajectories in single and multipost environments are shown in Figs. 2(b) and 2(c). To characterize the interactions between the robot and the post(s), the robot was initialized to always start in the same configuration: the "S" shape shown in Fig. 1(a). The robot was then placed so that its head was within a box of dimension $L_x \times L_z$, where L_x is set by either the amplitude of the robot (single post) or the center-to-center distance between posts (multipost) and L_z is set by the distance traveled by the robot in a single undulation cycle (see Fig. 2). Outside this region, interactions would either be repeated or the snake would always entirely miss the post.

Multibody physics simulations, created with Chrono [42], allowed for parameter variation and provided additional information (such as time-resolved forces on the robot) not available from the experiment. Experimentally validated simulations were created using the physical parameters of the experiment and the wheel friction relations in Fig. 1(c). The resulting simulations were in good agreement with experiments [40].

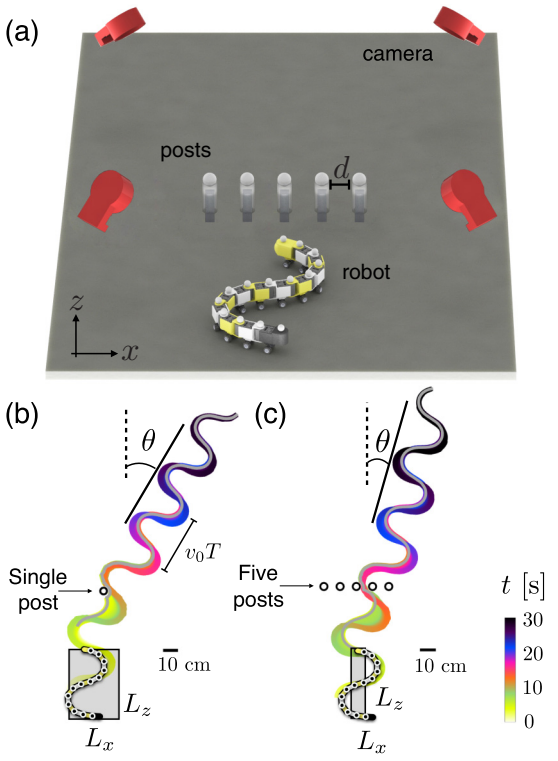

FIG. 2. Single- and multipost experimental configurations. (a) Schematic of the arena. Cylindrical vertical posts (radius $r = 4.5$ cm) were rigidly affixed to an otherwise homogeneous substrate. In the single-post case, only the central post was present. For multipost experiments, a row of evenly spaced posts were oriented transverse to the robot's initial direction of travel. (b) Snapshots of robot configurations and locations (colored by time) throughout an interaction with the single post. (c) Snapshots of robot configurations and locations throughout an interaction with multiple posts, colored by time. The gray line shows the trajectory of the head. In both cases, interactions with the post(s) deflect the robot's heading by an angle θ.

III. RESULTS AND DISCUSSION

A. Single post: Scattering distribution

We began with a simple heterogeneous terrain: a single vertical post firmly anchored to an otherwise homogeneous substrate [see Fig. 2(a)—for these experiments, only the central post was present in the arena]. We find that collisions with the post rotate the robot's direction of travel [Fig. 2(b)], and that, given the low-slip interaction with the substrate, the full trajectory is well approximated by the path traced by the head. We therefore used the head trajectory to describe the robot's dynamics.

To visualize how collisions affect the spatial distribution of trajectories beyond the post, we generated a *probability map*, i.e., a statistical image in which each pixel value indicates the fraction of trials the corresponding region in space was traversed by the robot. Figures 3(a) and 3(b) reveal that a structured pattern emerges in both experiment and simulation when initial conditions are densely sampled.

Two notable features in these probability maps are quite different from what we would expect from simple collisions in nonactive systems. First, there are periodic excluded regions ("images" of the post) beyond and directly behind the post, which are reminiscent of features in near-field diffraction patterns. Here these excluded regions occur at integer multiples of v_0T [the distance traveled in a single undulation cycle, see Fig. 2(b)]. These forbidden regions arise from the low slip trajectory enforced by the wheels and the physical constraint that the robot cannot penetrate or move the post. While excluded regions could arise in nonactive collisions, the structure would be different. For instance, in the predicted

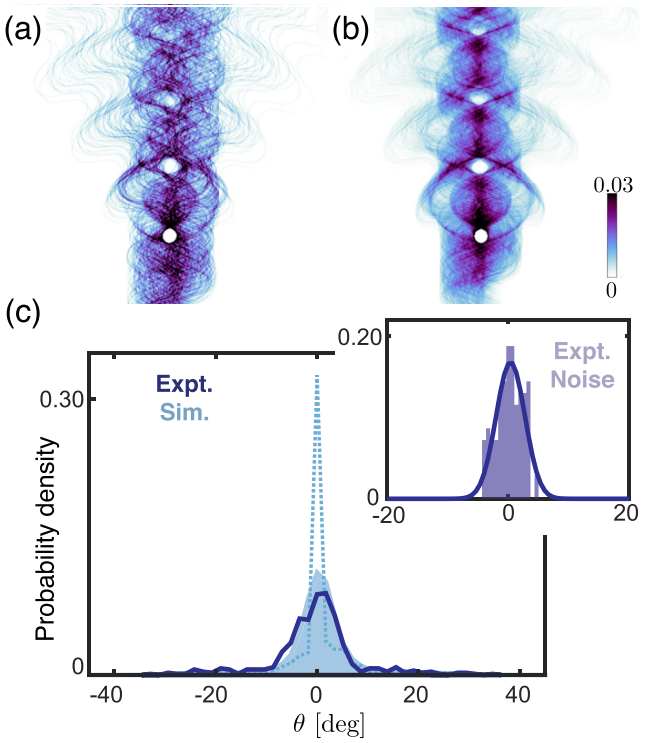

FIG. 3. Single-post scattering patterns and distributions. Probability maps of head trajectories for (a) 481 experimental and (b) 3000 simulated snake-post interactions. Here the color scale indicates fraction of trials passing through each pixel. (c) Scattering angle distributions for both experimental (dark blue curve) and simulated (dashed light blue curve) snake-post interactions with a single post. Inset: The shaded region shows trajectory angles for 104 experiments in which the robot did not interact with the post. The curve shows a normalized Gaussian fit to the data, with mean $\theta_0 = 0.4^\circ \pm 0.1^\circ$ and standard deviation $\sigma_\theta = 2.4^\circ \pm 0.1^\circ$. Uncertainty in fit parameters indicate 95% confidence intervals. To estimate the effect of the experimental error in robot placement would have on the simulation distribution, a noise value was drawn from the Gaussian fit and added to each simulation scattering angle. This process was repeated 10 000 times, and the resulting simulation distribution is the shaded blue region.

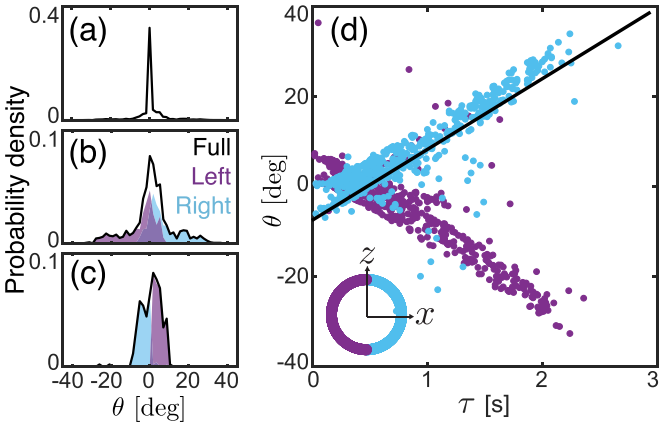

FIG. 4. Single-post interactions. (a) Scattering angle distributions including 3000 simulations; (b) the simulations in which the robot's head collided with the post (about 40%); (c) simulations which involved only nonhead interactions (about 10%). The remaining 50% did not interact with the post. The black outlines show the full distribution for each case, and the colored subdistributions indicate how the robot scattered based on which side of the post was hit. (d) For interactions which involved the head of the robot, the resulting scattering angle varies linearly with the duration of the head-post contact. The inset shows a schematic of the post, oriented so that the initial robot heading is along $+\hat{z}$. Colors of points in the main plot are consistent with this schematic and indicate which side of the post was hit. The solid black line shows a linear fit to the blue points.

scattering pattern of a ball initially traveling along a straight path toward a fixed obstacle, momentum-conserving final trajectories would either miss the obstacle completely or bounce off and scatter backward. In contrast, we find that no single robot trial results in back-scattering or reflection; in all cases, the internal driving ensures that the robot continues to travel forward after the interaction.

Second, we find that most interactions produce small deflections, which we quantify by measuring the scattering angle, θ [defined in Fig. 2(b)], of all trajectories. Distributions of θ values for both experiments and simulations have a central peak which confirms that $\theta = 0^\circ$ is the most probable deflection [see Fig. 3(c)]. Distributions show that $\theta = 0^\circ$ occurs more often in the simulation; however, we find that agreement can be improved by accounting for experimental error associated with manual initial placement of the robot at the beginning of each experiment [see inset of Fig. 3(c)]. When noise representative of this experimental error is added to the simulated scattering angles, we recover a simulation distribution in good agreement with that of the experiment.

B. Single post: Individual collisions

To understand how robot-post interactions contribute to the scattering distribution, we used simulations to investigate individual collisions. Robot-post interactions were identified by nonzero contact forces on robot body segments. Approximately half of all simulations have no interaction, ∼40% experienced a head-post collision, and the remaining ∼10% had only nonhead interactions [see Figs. 4(a)–4(c)]. Unlike collisions in nonactive systems, scattering distributions that only include robot-post interactions remain strongly peaked around no deflection. Additionally, nearly all simulations with a head-post interaction were *repulsive* (robot deflected away from the post), and simulations with only nonhead interactions were *attractive* (robot deflected inward toward the post), analogous to Ref. [37].

Given that most interactions included a head-post collision and that the low-slip trajectory ensures that body segments follow the path traced by the head of the robot, we focused on head-post collisions and used the head trajectory to describe interaction dynamics. To quantify the persistence of this interaction, we define the head-post contact duration, $\tau = t_f - t_0$, where t_0 and t_f are the initial and final times of contact, respectively. Figure 4(d) shows that scattering angle, θ, varies linearly with τ.

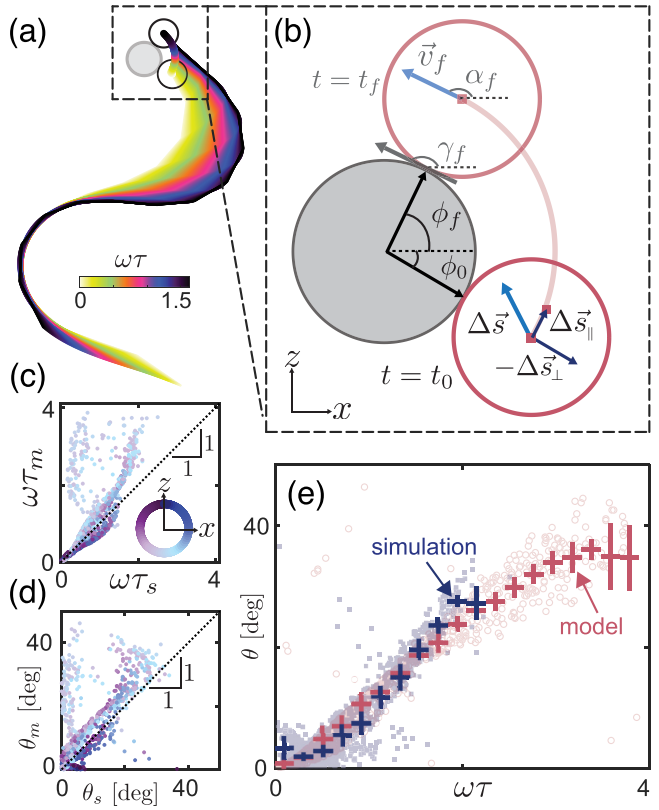

FIG. 5. Collision model. (a) Snapshots of the full body of the simulated snake throughout the collision. (b) Model for head-post interaction. (c) Comparison between model predicted and simulation contact durations. Color indicates initial collision location on post, which is labeled in the inset. Most data fall along the $\omega\tau_m = \omega\tau_s$ line, with discrepancies arising for collisions near the leading edge of the post. (d) Comparison between model predicted and simulation scattering angles, colored by initial contact location. (e) Scattering angle vs. contact duration for both simulation and model. Light points show raw data. Dark crosses show averaged θ values within $\omega\tau$ bins. Horizontal lines indicate bin widths, and vertical lines show standard deviations.

C. Single post: Active collision model

The time evolution of a representative head-post interaction is shown in Fig. 5(a): As the head moves along the post surface, the body-ground contact locally slips and causes a rigid rotation of the entire body. These observations motivate a simple model in which we treat the head as a self-propelled circular particle, illustrated in Fig. 5(b). We prescribe a time-dependent driving velocity, $\vec{v}(t)$, that matches the unobstructed head velocity. Particle-post contact is established upon initial overlap and is maintained until the particle velocity vector no longer has a component which points in toward the center of the post (i.e., contact ends when $\hat{v} \cdot \hat{r} > 0$, where $\hat{r}$ points radially outward from the post center). During this contact, the particle incrementally moves along the post surface by an amount

$$\Delta s_\parallel(t) = c_1 v_\parallel(t)\Delta t, \tag{1}$$

where $v_\parallel(t)$ is the component of $\vec{v}(t)$ that is locally tangent to the post surface at time t and c_1 is a constant that should be related to the post-particle friction coefficient (here we find good model-simulation agreement for $c_1 = 1$). While we did not vary the friction coefficient, we expect that c_1 should be inversely related to the head-post static friction, μ_s: for $\mu_s \to \infty$, $c_1 \to 0$ and for $\mu_s \to 0$, $c_1 \to 1$. In simulations presented here, $\mu_s = 0$.

As the particle advances along the post surface, the rigid and impenetrable post requires that the velocity component perpendicular to the post must be 0. However, there is a nonzero component to the driving force which would have advanced the particle by an amount

$$\Delta s_\perp(t) = v_\perp(t)\Delta t \tag{2}$$

in a homogeneous environment. Given that this motion cannot occur, we suppose that the post effectively pushed the freely moving particle by a distance $-\Delta s_\perp$ to maintain its location at the post surface and that this push resulted in an infinitesimal rotation,

$$\Delta\theta(t) \sim -\Delta s_\perp(t)/r_{\text{eff}}, \tag{3}$$

about a point some distance r_{eff} away from the contact point. If r_{eff} is constant, then the model-predicted scattering angle, θ_m, is determined by summing incremental $\Delta s_\perp(t)$ over the duration of the contact.

Figure 5(c) compares the model-predicted and simulation contact durations. Data are clustered around the $\omega\tau_m = \omega\tau_s$ line, showing that the model predicts the duration in most cases. Discrepancies are caused by the model requirement that $\vec{v}_\parallel \cdot \hat{z} \geqslant 0$ (i.e., the particle cannot travel backward along the surface). While this rule produces good agreement between the model and the simulation in most cases, we find that there is a small region at the leading tip of the post in which this rule does not accurately describe the dynamics. In these cases, the simulated snake head can have a small negative v_z, allowing it to slide backward and around the leading tip of the post, and resulting in a quickly broken contact. In the model, however, the particle is pinned at the same location until the velocity reorients and the particle slides along the post in the $+\hat{z}$ direction. We find that these points always produce the largest discrepancies between the model and simulation. We expect that a better rule to describe these interactions would improve the agreement between the simulation in this region.

To predict a scattering angle from the model, we assume that r_{eff} is constant and related to λ_{snake}, the wavelength of the snake, and we combine Eqs. (2) and (3) to obtain

$$\theta_m = \frac{c_2}{\lambda_{\text{snake}}} \int_{t_0}^{t_f} -v_\perp(t)dt, \tag{4}$$

where θ_m is the model-predicted scattering angle and c_2 is a constant of proportionality. To estimate the value of c_2, we compared the right-hand side of Eq. (4) to simulation scattering angles, θ_s. We find that $c_2 \approx 1$ produces a good match. Figure 5(d) compares the resulting model-predicted θ_m values with the corresponding θ_s values. Most data cluster around the $\theta_m = \theta_s$ line, indicating that the simplified picture provided by the model is a reasonable approximation for the observed dynamics of most collisions.

Next, we compare the predicted dependence of the scattering angle on the contact duration in Fig. 5(e). The model

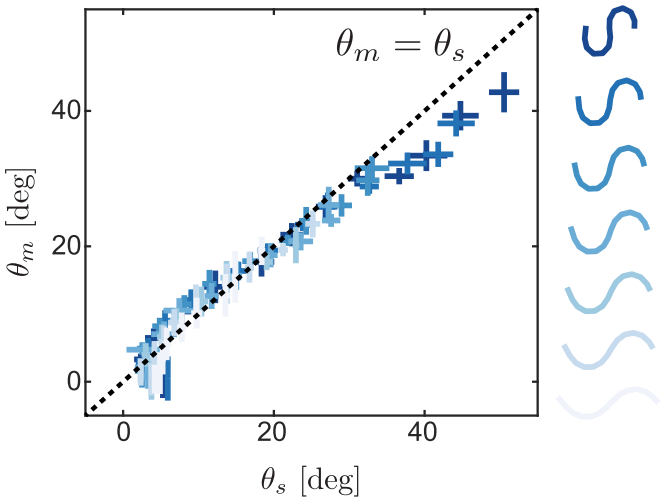

FIG. 6. Snake shape variation. The model-predicted scattering angle, θ_m, compared with simulation scattering angles, θ_s. Colors represent different shapes, labeled to the right of the main plot. For each shape, θ_m is predicted for each simulation. To make comparison easier, θ_m and θ_s values shown were averaged within identical $\omega\tau$ bins. Error bars indicate the standard deviations within each bin.

captures the observed trend: θ varies linearly with τ. Given the density of the raw data, we divided the data into windows based on $\omega\tau$ values and averaged all θ values within each bin. These averaged values are in good agreement.

To test the generality of Eq. (4), we ran simulations for different snake shapes. By varying the angular amplitude of the motor oscillations, $\zeta_{\max}$, we change both the amplitude of the overall wave shape as well as the wavelength of the snake. Using the model, we again determine the right-hand side of Eq. (4) and compare with the scattering angles measured from the simulation. We find that $c_2 \approx 1$ produces good agreement across amplitude variations investigated here. To demonstrate this agreement, we again compute the average predicted and simulated scattering angles within $\omega\tau$ bins, as in Fig. 5(e). Figure 6 shows these average scattering angle values plotted against each other. All values fall close to the line $\theta_m = \theta_s$, indicating that the model is valid over the range of amplitudes explored here.

We next explore how the dynamics depend on physical parameters not varied in the simulation. We therefore investigate how variation in head-post friction, μ_s, head size, r_{head}, post size, r_{post}, and driving speed, v, affect scattering distributions. From geometry, we know that $\Delta s_{\parallel} = (r_{\text{head}} + r_{\text{post}})\Delta\phi$, which, when combined with Eq. (1), along with the fact that $v_{\parallel} \leqslant v$ and the expectation that $c_1 \sim 1/\mu_s$ yields

$$\Delta\phi \leqslant \frac{v}{\mu_s(r_{\text{head}} + r_{\text{post}})}\Delta t, \tag{5}$$

where $\Delta\phi$ is the incremental change in post contact location that occurred over time Δt. From this relation, the model predicts that if Δt, v, and $r_{\text{head}} + r_{\text{post}}$ are constant, then as $\mu_s \to \infty$, $\Delta\phi \to 0$. Given that there are more states for which the velocity orientation can meet or exceed tangency as the particle approaches the trailing tip of the post, this reduction in $\Delta\phi$ means that the particle may either require more time to reach the trailing edge of the post or, alternatively, require more time to achieve tangency at points closer to the leading tip of the post. In either case, this can lead to longer contact durations, which we know from Fig. 5(e) produce larger deflection angles. Therefore, we expect the distribution of scattering angles to broaden as head-post friction increases. Similarly, if we fix μ_s and vary $r_{\text{head}} + r_{\text{post}}$, then we expect that for a larger diameter post or a larger diameter head, $\Delta\phi$ will again decrease, which will broaden the distribution of scattering angles. Finally, increasing the driving speed with other parameters held constant could enable the particle to overcome higher friction or larger obstacles.

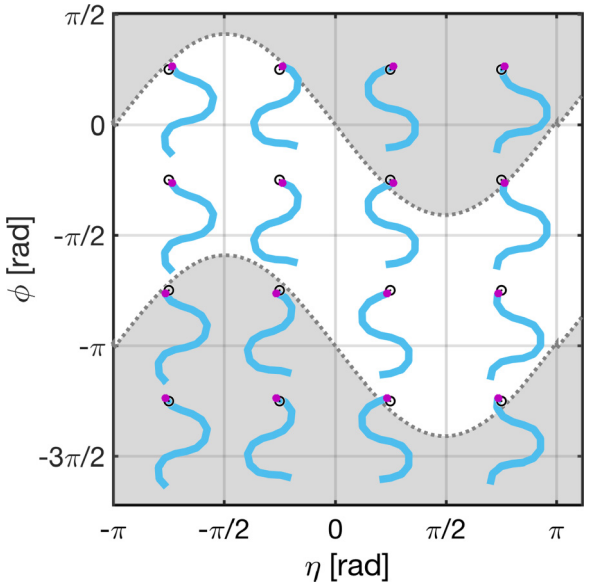

FIG. 7. Single-post collision state space. Sketches depicting snake configuration and impact location for single-post collision states. The shaded gray region indicates states that are not allowed because they require the robot to travel through the post to reach the correct configuration.

D. Single post: Collision state space

The simplified picture of the model provides insight into the dynamics of undulatory active collisions. In particular, persistent interactions with obstacles lead to locomotor deflections, which are set by the duration of the head-obstacle contact. From the model, we find that the duration of the contact is set by the initial collision state, which is defined by the initial location on the obstacle and the velocity orientation at impact. Therefore, rather than xz space, we choose a more natural collision state space. We define the initial contact point by the angular location on the post, ϕ, and we choose to define the velocity in terms of a wave phase, η, over velocity vector orientation, because the phase uniquely specifies location in the undulation cycle. Given that the primary oscillation direction is transverse to the average heading, which is initially in the $+z$ direction, we define the phase as $\eta = \tan^{-1}(\dot{x}/\omega x)$. For more information about how points are mapped from xz space to $\eta\phi$ space, see Ref. [40].

Figure 7 depicts the physical configuration of the snake and the post for several of these collision states. Accessing the

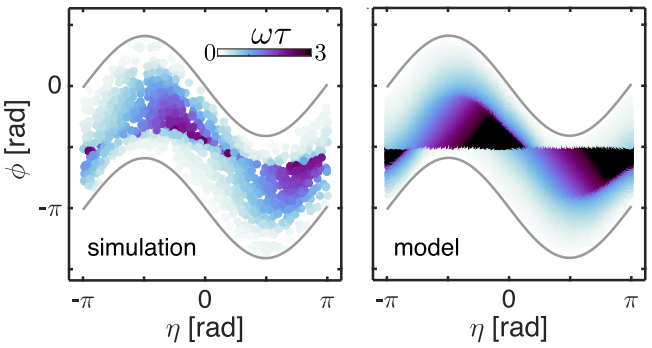

FIG. 8. Single post collision states and durations. Impact location, ϕ, and wave phase, η, colored by the duration of the resulting head-post collision for 1200 simulations (left) and predicted for 85 000 points (right).

states in the shaded gray regions would require the robot to travel through the post; therefore, these states are forbidden. States within the white band are allowed, and the dashed line between the two regions indicates the boundary between allowed and disallowed states.

We use the model to predict $\omega\tau$ for all possible collision states, and we compare with results from simulation in Fig. 8(a). The structure of $\omega\tau$ as a function of η and ϕ is qualitatively similar: Both are contained within the same region, whose boundaries are identical to those of Fig. 7, and while there are quantitative differences between the simulation and the prediction [40], the dependence of the duration on the collision state is qualitatively similar.

The model provides a framework for describing active collisions in damped-driven systems. Heterogeneities in the environment impose geometric constraints which can prevent active particles from fully utilizing their internal driving to produce movement. The degree to which obstacles hinder locomotion depends on the details of the driving and the shape of the obstacle: For an undulating locomotor interacting with round posts, we find that the duration of the interactions is set by the undulation phase and post impact location at the initial time of contact. The locomotor is "stuck" to and can only move along the surface of the obstacle until the velocity vector reorients and has a component pointing away from the obstacle. We note that, in this picture, the contact duration is qualitatively equivalent to the reorientation time of many other active matter systems (see, e.g., Ref. [22]). However, unlike active Brownian systems and those which experience a purely passive reorientation [23], the reorientation is largely inherent in the driving of the locomotor. For a periodically driven locomotor interacting with a single post, we find that

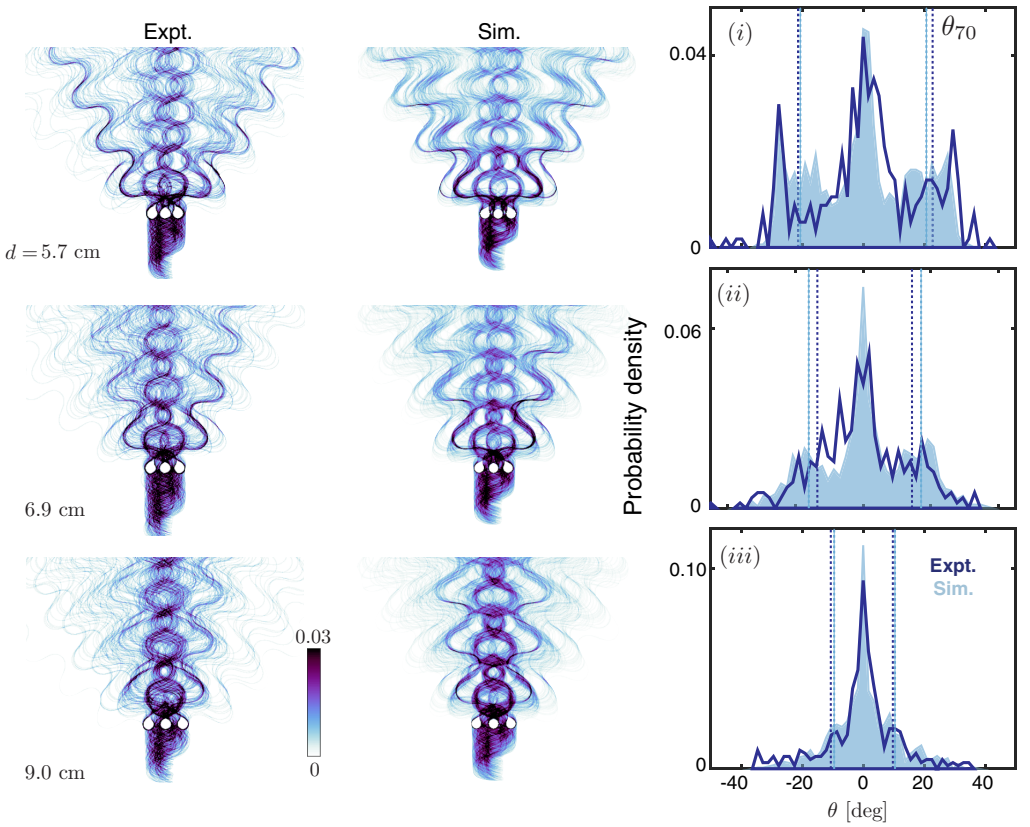

FIG. 9. Scattering patterns and distributions varying post spacing. Probability maps of robot head trajectories for three post configurations in experiment (left column) and simulation (middle column). Here the color scale indicates fraction of trials passing through each pixel. d is constant across each row and increases down each column. Right column: Experiment (dark blue curves) and simulation (shaded light blue regions) scattering angle distributions for three post spacings, $d = 5.7$ cm, $d = 6.9$ cm, $d = 9.0$ cm, each of which contains at least 300 trials. Dashed vertical lines show the angles associated with the outer $\pm 15\%$ of each distribution (i.e., the 15th and 85th quantiles).

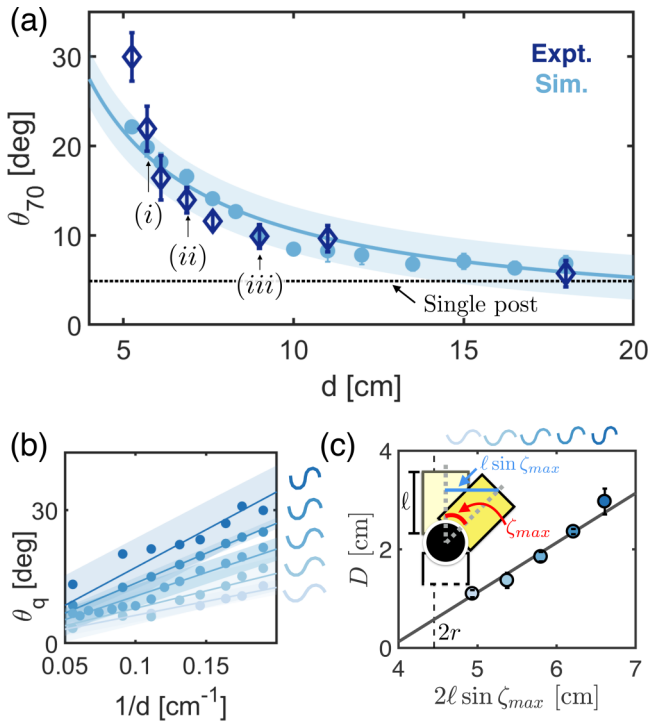

FIG. 10. Distribution spread dependence on post spacing and segment angular amplitude. (a) θ_{70} vs. d for experiment (dark diamonds) and simulation (light circles). Numerically labeled points result from corresponding distribution in Fig. 9. Error bars indicate bootstrapping-estimated 95% confidence intervals associated with each quantile measurement. The curve shows the fit of $\theta_{70} = 180/\pi\,(D/d)$ to the simulation, with the shaded region indicating the 95% prediction bounds for the fit. (b) θ_{70} vs. $1/d$ measured from distributions for different $\zeta_{\max}$ (varied in simulation). Lines show fits to the data, and shaded regions indicate 95% prediction bounds for each fit. Corresponding wave shapes are shown to the right. (c) The fit parameter, D, for different $\zeta_{\max}$. D is linearly related to the full perpendicular distance each segment sweeps out in one period. Inset: schematic of single motor and two adjacent segments. The perpendicular distance swept out by a single segment during a full cycle is given by $2\ell \sin \zeta_{\max}$.

collision durations (and corresponding locomotor reorientations) increase as initial impact locations approach the leading edge of the post.

E. Multiple posts: Scattering distributions

We next explore how the presence of multiple obstacles alters scattering distributions and underlying collision states. Here five evenly spaced vertical posts were firmly anchored to an otherwise homogeneous substrate [a schematic is shown in Fig. 2(a)]. A representative experimental trajectory is shown in Fig. 2(c). Similarly to the single-post interactions, here the robot is rotated by the collisions with the posts. A probability map of multipost trajectories shows the likelihood of the robot to occupy points in space after the collision (Fig. 9). When the initial conditions were densely sampled (shown in the left and central columns), a structured pattern appeared and the presence of preferred trajectories emerged.

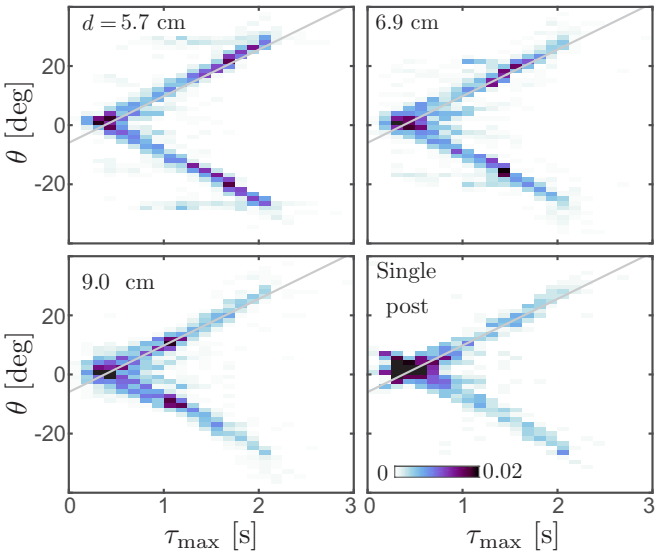

FIG. 11. Scattering angle dependence on head-post contact duration. Scattering angle, θ, depends linearly on $\tau_{\max}$, the longest head-post contact duration, even in the presence of multiple posts. The gray line, determined by fitting the single-peg data in the bottom right, is the same in all plots and shows that this trend is independent of post spacing, d. The underlying color scale represents the two-dimensional probability map and shows that the density of points shifts inward along the θ vs. τ line as spacing increases. The plot in the bottom right shows the probability map version of the single post data shown in Fig. 4(b).

Probability maps and their corresponding scattering angle distributions (Fig. 9) reveal that all θ distributions have a central peak around zero and are symmetric. We observe distinct secondary peaks for small d; as d increases, these off-center peaks become less prominent and eventually vanish, leaving only the central peak. Given this qualitative change in the structure of these distributions, we measure the overall spread of the distribution using the quantile value, θ_q (the θ value for which q% of the distribution is below θ_q). Since the θ distribution is nearly symmetric about 0, we compute θ_{70} for the $|\theta|$ distribution.

Figure 10(a) shows that θ_{70} values decrease with increasing d, confirming that the weight of the distributions shifts inward as spacing increases. The dependence of θ_{70} on the post spacing is well described by the function $\theta_{70} = (180/\pi)(D/d)$, where D is a fit parameter. The qualitative structure of these distributions is reminiscent of diffraction and, remarkably, the functional form of the fit describing the dependence on post spacing is similar to the form expected for far-field diffraction [43]. Variation of $\zeta_{\max}$ [defined in Fig. 1(b)] in simulation reveals that this functional form is valid over an intermediate range of shapes [see Fig. 10(b)], with D set by $2\ell \sin \zeta_{\max}$, the distance (along the post-plane direction) swept out by each segment during a single period [see Figs. 10(b) and 10(c)]. Outside this intermediate $\zeta_{\max}$ range, the spacing dependence is qualitatively different [40].

Features of these scattering distributions are a consequence of persistent collisions that arise in driven systems: First, even when interacting with multiple posts, there is a strong central peak; second, large reorientations are more frequent for small

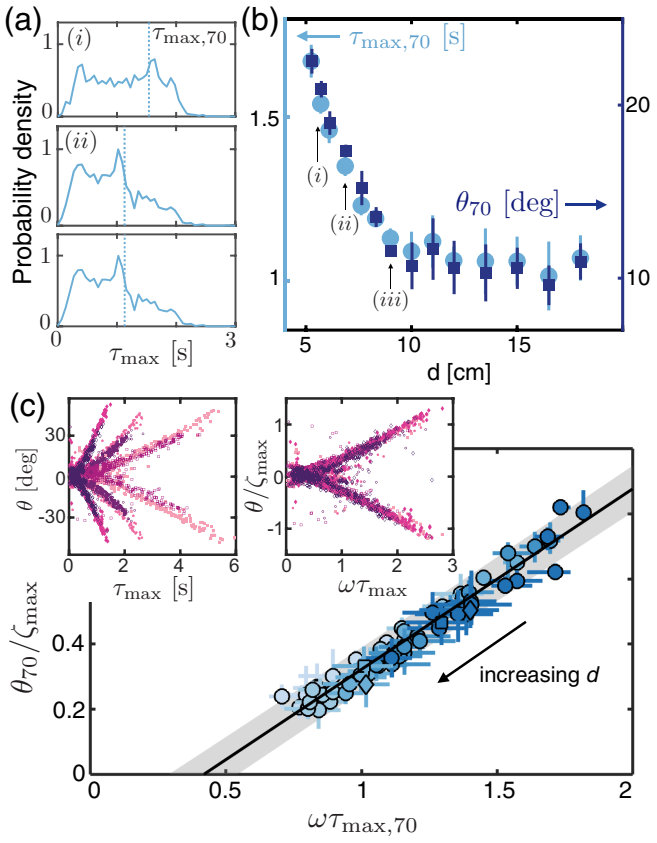

FIG. 12. Collision duration sets reorientation. (a) Probability distributions of the maximal contact duration, $\tau_{\max}$, for three post configurations (with spacing increasing down the column). Vertical lines show $\tau_{\max,70}$, the 70th quantile of each $\tau_{\max}$ distribution, which decreases as d increases [$(i) \rightarrow (iii)$]. (b) The spacing dependence of $\tau_{\max,70}$ (light blue, left axis) and θ_{70} (dark blue, right axis). Here distributions only include simulations for which there was a head-post collision. Error bars show the bootstrapping-estimated 95% confidence interval for each value. (c) θ_{70} and $\tau_{\max,70}$ (nondimensionalized by $\zeta_{\max}$ and ω, respectively) plotted against each other, shows the dependence can be described by a single line (of slope 0.55 ± 0.03 and y intercept -0.23 ± 0.04) over a range of $\zeta_{\max}$ (indicated by color and consistent with Fig. 10), f (□ : 0.075 Hz; ○ : 0.15 Hz; ◇ : 0.3 Hz), and d. Inset: θ vs. τ for $\zeta_{\max} = 0.605$ rad (dark open symbols) and $\zeta_{\max} = 0.705$ rad (light filled symbols) for raw (left) and nondimensionalized (right) data. Symbols indicate frequency and are consistent with main plot.

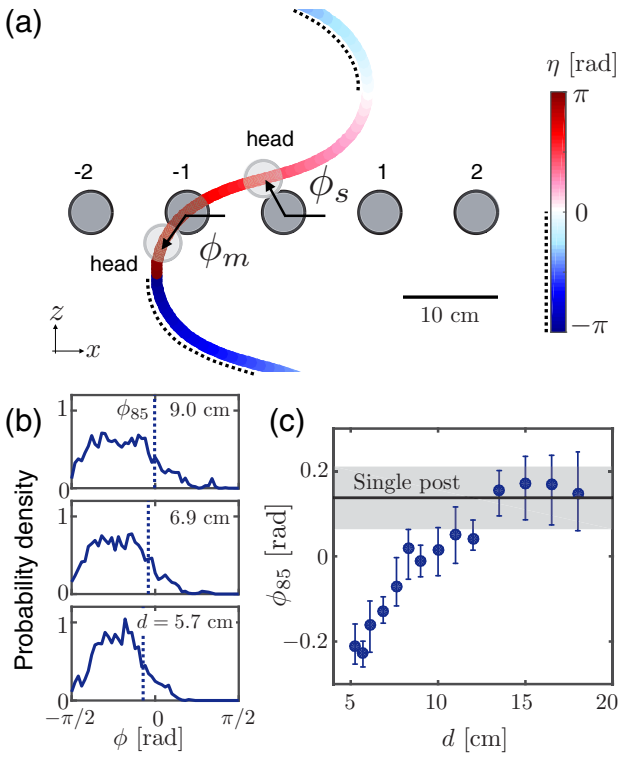

FIG. 13. Multipost scattering results from shifted likelihood of single-post collision states. (a) Post impact location and wave phase at collision are shifted when multiple posts are present. Lighter values show phase closer to zero, and the dashed line to the left of the curve identifies regions of the trajectory with negative phase. (b) ϕ distributions (reflected about $-\pi/2$) for three d. As d decreases (down the column), less of the peg surface is accessible to the robot, shifting the tails of the distributions toward the leading edge of the post. The vertical lines show ϕ_{85} (the 85th quantile), a measure of the tail of the ϕ distribution. (c) ϕ_{85} as a function of d. Error bars show the bootstrapping-estimated 95% confidence interval for each ϕ_{85} value.

d and tend to occur at preferred directions. This produces secondary peaks in the scattering distributions which become more prominent as spacing decreases.

F. Multiple posts: Collision durations

Given the importance of the head-post contact duration for the single-post environment, we again explore the relationship between the contact duration of the head with the posts. In the multipost geometry, the head can have multiple collisions which can involve more than one post. However, we find that there is typically one head collision that dominates; therefore, we start by examining the single collision with the maximal head-post contact duration, and we restrict our analysis to simulations which had at least one head-post collision [40].

Figure 11 shows that, even in the multipost configuration, θ depends linearly on $\tau_{\max}$ and that this relationship is independent of d. When each plot is viewed as a probability map, the dependence on d is clear: The density of points along this line shifts toward lower θ and $\tau_{\max}$ as d increases. Given this linear relationship, we expect that the spread of both the $\tau_{\max}$ and θ distributions should exhibit a similar dependence on spacing.

We explore this potential similarity by comparing the qualitative dependence $\tau_{\max}$ and θ quantiles on the spacing. Figure 12(a) shows distributions of $\tau_{\max}$ for three d. We again choose the 70th quantile to characterize the spread of the distributions. Figure 12(b) shows the qualitatively similar spacing dependence of $\tau_{\max,70}$ and θ_{70}. This correspondence is robust, holding over a range of undulation frequencies, f, and angular amplitudes, $\zeta_{\max}$. When θ_{70} and $\tau_{\max,70}$ distributions are scaled by $\zeta_{\max}$ and f, respectively, all data collapse to a single line, see Fig. 12(c).

We have neglected many details of the interactions that occur along the robot body as it traverses the post array

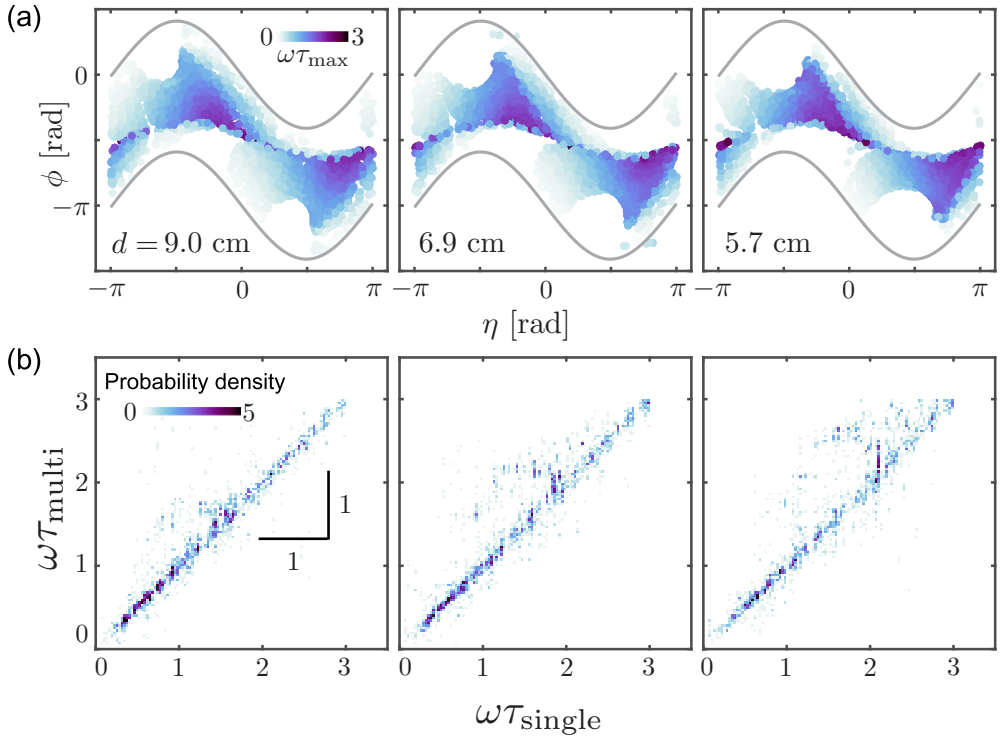

FIG. 14. Accessible collision states for different post spacing. (a) Possible collision states in (η, ϕ) space, colored by contact duration. As d decreases (left to right), fewer states are accessible. Gray lines indicate boundaries of possible states in the single-post scenario. (b) Probability map of multipost contact duration, $\omega\tau_{\text{multi}}$ as a function of $\omega\tau_{\text{single}}$ the duration of nearest single-post collision state in (η, ϕ) space.

and have shown that we can reduce the system to a single interaction: the longest-duration collision. Not only does this indicate that the resulting dynamics are dominated by the longest head-peg interaction, but it also suggests that, at least for our system, only one post is important in a given single- or multipost scattering event. It would be interesting to explore situations (for instance, trajectories with higher slip or a more complex arrangement of obstacles) in which there may be multiple important interactions.

G. Multiple posts: Collision states

To understand how active collisions in the presence of multiple posts can generate the observed scattering patterns, we examine the unobstructed path of the robot. This path is shifted to coincide with an initial condition that results in a collision for both $d = 5.7$ cm as well as for the single post, see Fig. 13(a). From this picture, we see that the single-post collision, which occurs opposite the leading surface of the central post, becomes inaccessible in the multipost scenario. Instead, a collision with the post immediately to the left precedes the single-post interaction. This new collision with an adjacent post occurs closer to the leading surface of the post, which, at least in the single post case, can result in a longer-duration collision.

We expect that as spacing decreases, states near the trailing edge of a post become inaccessible as these trajectories are intercepted by and occur closer to the leading edge of an adjacent post [see Fig. 13(a)]. To test this hypothesis, we quantified how the tail of the ϕ distribution depends on post spacing. Distributions for three d are shown in Fig. 13(b), and the dependence of ϕ_{85} on d is shown in Fig. 13(c). As predicted, the tails of these distributions shift toward the leading edge of the post as d decreases.

Not only was the impact location altered by the presence of multiple posts, but it is clear from Fig. 13(a) that the phase of the undulation cycle on impact was also changed. Scatter plots in Fig. 14(a) show how these collision states in (η, ϕ) space depend on spacing. As d decreases, fewer states are accessible to the robot, and the states that become inaccessible are those away from the leading edge of the post. Aside from this restriction on allowed states, the dependence of $\tau_{\max}$ on η and ϕ is nearly the same. This suggests that collision states are largely independent of d.

To test the similarity of collision states for different post configurations, we compare the single post collision state closest to [i.e., smallest Euclidean distance in the (η, ϕ) space from] each multipost state in (η, ϕ) space [40]. If the states are equivalent, then contact durations associated with the single and multipost state should be identical. Figure 14(b) shows the probability maps of three multipost durations as a function of the nearest single-post state. For all three d, most of the data fall along the $\omega\tau_{\text{multi}} = \omega\tau_{\text{single}}$ line, confirming that adjacent posts act primarily to shift the probabilities of single-post collision states. As the spacing decreases, single-post states near the trailing edge of the post occur with reduced probability (and some are even eliminated completely) as trajectories are "remapped" to a different single-post collision state occurring at an adjacent post. These shifted collisions tend to occur closer to the leading tip of the post than the

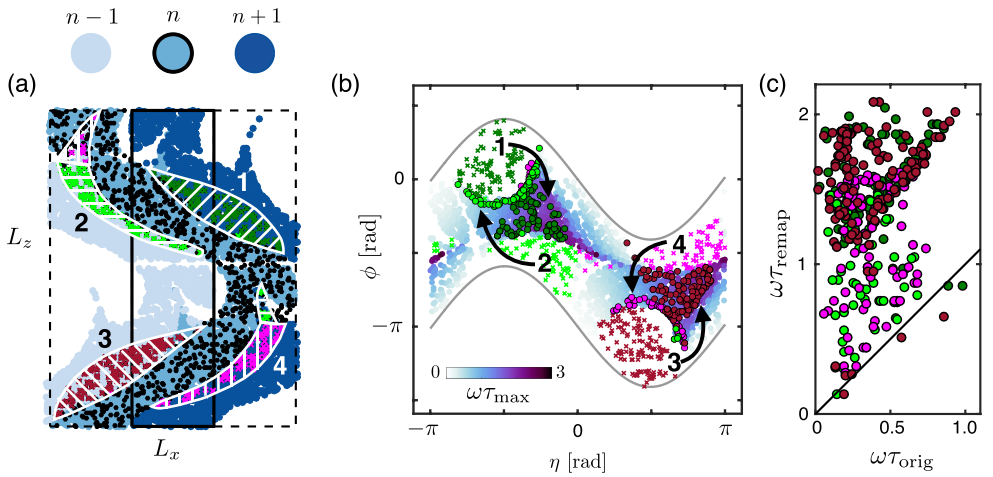

FIG. 15. Single-post states are shifted by the presence of multiple posts. (a) Tiled initial conditions for $d = 5.7$ cm are shown in light (left) to dark (right) blue, and single-post initial conditions are overlaid in black. All single-post points hit the central (and only) post present in that configuration, outlined in black. The color of the multipost initial conditions indicates which post was hit. The four numbered shaded areas containing "x" points indicate regions which no longer hit the central post when multiple posts were present. Instead, they collided with an adjacent post. (b) Multipost collision states in (η, ϕ) space, colored by duration of contact. The colored "x" regions here show the same four numbered regions highlighted in (a). Arrows indicate how regions of collision states are shifted by the presence of adjacent posts (from numbered "x" regions to ○ regions of the corresponding color). (c) In nearly all cases, the new collisions that occur on an adjacent post had significantly longer durations, τ_{remap}, than the original single-post collision, τ_{orig}. The line shows $\omega\tau_{\text{remap}} = \omega\tau_{\text{orig}}$.

original collision, often resulting in longer durations than the single-post state that was replaced. Given the linear relationship between duration and scattering angle, the remapping from shorter to longer durations shifts power from the central peak of the θ distributions out to the tails, creating and bolstering secondary off-center peaks.

To explore how single-post states are shifted by the presence of multiple posts, we identify the multipost point closest to each single post point in (x, z) space. To do this, we tiled the multipost initial conditions box [e.g., for $d = 5.7$ cm, the solid box in Fig. 15(a)] by shifting all points within this region over by $\pm mL_x$, where m is an integer and L_x is the transverse dimension of the initial conditions box. Outlines for shifts of $m = \pm 1$ are shown as the dashed boxes in Fig. 15(a). The points within each box show the starting point for the head of the robot, and the colors indicate which post was involved in the longest-duration collision with the head of the robot. When initial conditions were shifted, a different post was centered in front of the box, and given that all initial conditions boxes are identical, the post number associated with a collision in a box shifted by m post must also be shifted by m.

In Fig. 15(a), the multipost points for $d = 5.7$ cm are shown in varying shades of blue, and the single-post points (all of which hit the central post, outlined in black) are overlaid in black. To identify how the single post points were shifted around in (η, ϕ) space, we determined the xz distance between each single-post point and the nearest multipost point, $\delta_{xz} = \sqrt{(x_s - x_m)^2 + (z_s - z_m)^2}$, which was rarely larger than 0.5 cm. The colored "x" markers in Fig. 15(a) identify four regions which hit post n in the single-post case but were involved in more significant collisions with adjacent posts in the multipost case. How these regions were shifted around in (η, ϕ) space is shown in Fig. 15(b). The "x" points were shifted to the circular points of the same color. Figure 15(c) shows nearly all of the remapped points had significantly longer durations, τ_{remap}, than the duration of the original state in the single-post case, τ_{orig}.

These results confirm that single-post collision states are largely unaltered by the presence of multiple posts, even when d is small. Instead, multiple posts serve to restrict the collision states accessible to the robot. As d decreases, low-duration states occurring near the trailing edge of the posts become inaccessible and are replaced by longer-duration collisions near the leading edge of an adjacent peg. Stated another way, scattering events with small reorientations are preferentially remapped to larger-angle scattering events.

IV. SUMMARY AND CONCLUSIONS

The results presented here provide a striking example of the dynamics that can arise in self-propelled systems when environmental heterogeneities are present. To explore the nature of the interactions that can occur during undulatory self-propulsion, we created a robophysical snakelike robot which self-deforms by propagating a wave of joint-angle variations from head to tail. Passive wheels enable the robot to translate by creating a highly dissipative coupling between these self-deformations and the surrounding environment. We find that the nature of this dissipation is similar to that of both viscous fluids (relevant for swimmers in low Reynolds number fluids) and granular materials (relevant for movement on and within sand). This suggests that our results may be relevant to biological and artificial systems spanning a broad range of length scales and environments.

Interactions with a single obstacle (a rigid vertical post) scatter the robot, and, unlike simple collisions in nonactive systems, the distribution of scattering angles produced by interactions with a single post is strongly peaked directly behind the post. When multiple posts are present, secondary

peaks emerge and become more prominent as post density increases, producing scattering patterns reminiscent of far-field diffraction. Surprisingly, we find that the collisions are not altered by the presence of multiple posts; instead, the likelihood of collisions shifts so that there are more interactions which produce large-scattering events. In all cases, the resulting scattering angle is proportional to the head-post collision duration. A simple model reveals that this duration is similar to the reorientation times discussed in many other active matter systems (see, e.g., Ref. [22]) and sets the outcome of the interaction. This understanding provides a starting point for manipulating either locomotor behavior or the surrounding environment to produce a desired outcome.

Simulations allowed for broader parameter variation and revealed that, like movement through similarly highly dissipative environments, our results are independent of the frequency of undulation. That is, the linear relationship between the head-post contact duration, $\omega\tau_{\max}$, and the resulting scattering angle remains the same for a broad range of frequencies. Variation of the angular amplitude, $\zeta_{\max}$, also did not significantly alter the linear dependence between the duration and the scattering angle, suggesting that our results are valid for a range of waveforms and undulation frequencies. Our model, which only considers the head of the snake, confirms this and is able to predict contact durations over the range of amplitudes investigated. With the addition of a lever arm (i.e., an effective length about which the snake is rotated), the model predicts scattering angles over the range of amplitudes studied. Surprisingly, simulation and model-predicted scattering angles agree when the lever arm length is equal to the wavelength of the snake.

Broadly speaking, our results provide a new approach to modeling collisions in active systems within dissipative environments, which could be applicable to both deterministically and stochastically driven reorientations. In at least some situations, such as the system presented here, self-propelled agents can be reduced to driven particles which possess *effective* physical properties and follow simple collision rules that are set by geometric constraints of the environment. Extending our model to create a general framework which draws inspiration from systems with both particle-like characteristics and effective wave like properties may provide insight into a wide range of periodically driven systems. In particular, it would be interesting to explore the potential connections to other systems which produce similar scattering patterns, such as biological snakes in heterogeneous environments [14] and bouncing fluid droplets interacting with substrate disturbances that they create [44,45].

We close by noting that robophysics provides a useful approach for exploring the nature of active collisions across scales and environments because it enables controlled experiments and systematic parameter variation while avoiding the complexities and unknowns of numerical collision-modeling and the variability and controllability difficulties found in living systems. Robophysics is widely applicable and amenable to other modes of locomotion, body morphologies, and obstacle configurations and geometries. With an understanding of active collisions, these interactions could be used to mitigate or even utilize interactions with heterogeneities for different classes and environments for natural and artificial locomotors, e.g., in legged [12,46], undulatory [33,47], sidewinding [48], wheeled and tracked vehicles [49,50], and even aerial systems [51,52]. Alternatively, environments could be designed to direct the motion of self-propelled systems, for instance, to correct for (e.g., Ref. [7]) or selectively enhance scattering effects. Finally, structured environments could also be used to modify the duration of these interactions, which, given the importance of the interaction duration on the dynamics of active systems, could have broad implications for collective behavior in biological and artificial systems.

ACKNOWLEDGMENTS

The authors thank Gordon Berman, John Bush, Mike Chapman, Yves Couder, Paul Goldbart, Cristina Marchetti, Zeb Rocklin, Andy Ruina, and Paul Umbanhowar for insightful discussions; Kelimar Diaz, Nathan Hines, and Alex Hubbard for help with data collection; and the reviewers, whose feedback improved this manuscript. This work was supported by NSF PoLS PHY-1205878, PHY-1150760, CMMI-1361778, NSF CMMI-1635004 (A.P. and D.N.), ARO W911NF-11-1-0514, ARL MAST CTA, NDSEG 32 CFR 168a (P.E.S.), DARPA YFA, and Dunn Family Professorship (D.I.G.). Data are available from the corresponding author on request.

[1] P. Holmes, R. J. Full, D. Koditschek, and J. Guckenheimer, SIAM Rev. **48**, 207 (2006).

[2] A. E. Hosoi and D. I. Goldman, Annu. Rev. Fluid Mech. **47**, 431 (2015).

[3] S. Childress, A. Hosoi, W. W. Schultz, and J. Wang, *Natural Locomotion in Fluids and on Surfaces: Swimming, Flying, and Sliding*, Vol. 155 (Springer, Berlin, 2012).

[4] M. C. Marchetti, J. F. Joanny, S. Ramaswamy, T. B. Liverpool, J. Prost, M. Rao, and R. A. Simha, Rev. Mod. Phys. **85**, 1143 (2013).

[5] K. Drescher, J. Dunkel, L. H. Cisneros, S. Ganguly, and R. E. Goldstein, Proc. Natl. Acad. Sci. USA **108**, 10940 (2011).

[6] J. Palacci, S. Sacanna, A. P. Steinberg, D. J. Pine, and P. M. Chaikin, Science **339**, 936 (2013).

[7] V. Kantsler, J. Dunkel, M. Polin, and R. E. Goldstein, Proc. Natl. Acad. Sci. USA **110**, 1187 (2013).

[8] P. D. Frymier, R. M. Ford, H. C. Berg, and P. T. Cummings, Proc. Natl. Acad. Sci. USA **92**, 6195 (1995).

[9] D. Takagi, J. Palacci, A. B. Braunschweig, M. J. Shelley, and J. Zhang, Soft Matter **10**, 1784 (2014).

[10] C. Reichhardt and C. J. Olson Reichhardt, Phys. Rev. E **90**, 012701 (2014).

[11] J.-C. Latombe, *Robot Motion Planning*, Vol. 124 (Springer Science & Business Media, New York, 2012).

[12] C. Li, A. O. Pullin, D. W. Haldane, H. K. Lam, R. S. Fearing, and R. J. Full, Bioinspir. Biomim. **10**, 046003 (2015).

[13] J. C. Spagna, D. I. Goldman, P.-C. Lin, D. E. Koditschek, and R. J. Full, Bioinspir. Biomim. **2**, 9 (2007).

[14] P. E. Schiebel, J. M. Rieser, A. M. Hubbard, L. Chen, Z. Rocklin, and D. I. Goldman, Proc. Natl. Acad. Sci. USA (to be published).
[15] K. Kelley, S. Arnold, and J. Gladstone, Funct. Ecol. **11**, 189 (1997).
[16] S. Park, H. Hwang, S.-W. Nam, F. Martinez, R. H. Austin, and W. S. Ryu, PloS ONE **3**, e2550 (2008).
[17] T. McGeer, Int. J. Rob. Res. **9**, 62 (1990).
[18] M. J. Coleman and A. Ruina, Phys. Rev. Lett. **80**, 3658 (1998).
[19] U. Saranli, M. Buehler, and D. E. Koditschek, Int. J. Rob. Res. **20**, 616 (2001).
[20] B. McInroe, H. C. Astley, C. Gong, S. M. Kawano, P. E. Schiebel, J. M. Rieser, H. Choset, R. W. Blob, and D. I. Goldman, Science **353**, 154 (2016).
[21] F. Qian and D. I. Goldman, Proc. SPIE **9467**, 94671U (2015).
[22] C. Bechinger, R. Di Leonardo, H. Löwen, C. Reichhardt, G. Volpe, and G. Volpe, Rev. Mod. Phys. **88**, 045006 (2016).
[23] G. Thoms, S. Yu, Y. Kang, and C. Li, in *APS Meeting Abstracts* (2017), http://meetings.aps.org/Meeting/MAR17/Session/Y12.9.
[24] J. Gray, J. Cell Sci. **s3-94**, 551 (1953).
[25] J. Gray and G. Hancock, J. Exp. Biol. **32**, 802 (1955).
[26] J. Gray and H. W. Lissmann, J. Exp. Biol. **41**, 135 (1964).
[27] M. Sfakiotakis, D. M. Lane, and J. B. C. Davies, IEEE J. Oceanic Eng. **24**, 237 (1999).
[28] G. B. Gillis, Am. Zool. **36**, 656 (1996).
[29] G. Juarez, K. Lu, J. Sznitman, and P. E. Arratia, Europhys. Lett. **92**, 44002 (2010).
[30] R. D. Maladen, Y. Ding, C. Li, and D. I. Goldman, Science **325**, 314 (2009).
[31] S. S. Sharpe, S. A. Koehler, R. M. Kuckuk, M. Serrano, P. A. Vela, J. Mendelson, and D. I. Goldman, J. Exp. Biol. **218**, 440 (2015).
[32] S. R. Lockery, K. J. Lawton, J. C. Doll, S. Faumont, S. M. Coulthard, T. R. Thiele, N. Chronis, K. E. McCormick, M. B. Goodman, and B. L. Pruitt, J. Neurophysiol. **99**, 3136 (2008).
[33] T. Majmudar, E. E. Keaveny, J. Zhang, and M. J. Shelley, J. R. Soc. Interface **9**, 1809 (2012).
[34] J. Gray and H. W. Lissmann, J. Exp. Biol. **26**, 354 (1950).
[35] C. Gans, Am. Zool. **15**, 455 (1975).
[36] J. Aguilar, T. Zhang, F. Qian, M. Kingsbury, B. McInroe, N. Mazouchova, C. Li, R. Maladen, C. Gong, M. Travers, R. L. Hatton, H. Choset, P. B. Umbanhowar, and D. I. Goldman, Rep. Prog. Phys. **79**, 110001 (2016).
[37] F. Qian and D. I. Goldman, Robotics: Science and Systems, 1 (2015).
[38] S. Hirose, *Biologically Inspired Robots: Serpentile Locomotors and Manipulators* (Oxford University Press, Oxford, 1993).
[39] S. Hirose and H. Yamada, IEEE Robot. Automat. Mag. **16**, 88 (2009).
[40] See Supplemental Material at http://link.aps.org/supplemental/10.1103/PhysRevE.99.022606 for further experiment and simulation details, simulation validation details, number and duration of head collisions as a function of d, densities of collision states as a function of d, and distances between nearest single and multipeg states.
[41] G. Batchelor, J. Fluid Mech. **44**, 419 (1970).
[42] A. Pazouki, M. Kwarta, K. Williams, W. Likos, R. Serban, P. Jayakumar, and D. Negrut, Phys. Rev. E **96**, 042905 (2017).
[43] We note the small angle approximation ($\sin\theta \approx \theta$) is valid for angles we measure, so a fit to the function expected for far-field wave diffraction, $\theta_{70} = 180/\pi \sin^{-1}(D/d)$, is indistinguishable from the fit we have chosen.
[44] Y. Couder and E. Fort, Phys. Rev. Lett. **97**, 154101 (2006).
[45] J. W. M. Bush, Annu. Rev. Fluid Mech. **47**, 269 (2015).
[46] C. Li, T. Zhang, and D. I. Goldman, Science **339**, 1408 (2013).
[47] B. C. Jayne, Copeia **1986**, 915 (1986).
[48] H. Marvi, C. Gong, N. Gravish, H. Astley, M. Travers, R. L. Hatton, J. R. Mendelson, H. Choset, D. L. Hu, and D. I. Goldman, Science **346**, 224 (2014).
[49] K. Iagnemma, D. Golda, M. Spenko, and S. Dubowsky, in *Experimental Robotics VIII*, edited by B. Siciliano and P. Dario (Springer, Berlin, Heidelberg, 2003), pp. 654–663.
[50] J. Y. Wong, *Terramechanics and Off-road Vehicle Engineering: Terrain Behavior, Off-road Vehicle Performance and Design* (Butterworth-Heinemann, London, 2009).
[51] D. Floreano, J.-C. Zufferey, M. V. Srinivasan, and C. Ellington, *Flying Insects and Robots* (Springer, Berlin, 2010).
[52] M. Turpin, N. Michael, and V. Kumar, Autonom. Robots **33**, 143 (2012).

SUPPLEMENTARY INFORMATION

The dynamics of scattering in undulatory active collisions

Jennifer M. Rieser, Perrin E. Schiebel, Arman Pazouki, Feifei Qian, Zachary Goddard,
Kurt Wiesenfeld, Andrew Zangwill, Dan Negrut, Daniel I. Goldman

1. Experiment

Our 13-segment-robotic snake, shown in Fig. 1a, had 12 Dynamixel AX-12A servo motors connected together with custom-designed 3D-printed plastic brackets, and a Robotis CM-700 controller was programmed to command the angular position of each motor to vary sinusoidally with time and position along the body. Robot segments were 3.7 cm wide, and 3-cm tall all interior segments were 5.1 cm long. The head, 6.0 cm long, added a nearly-spherical nose cap to the interior segment design, and the tail, 7.5 cm long, was adapted to have a cylindrical cap. The robot mass was 1.13 kg and the fully-extended length was around 80 cm.

The snake moved in a model heterogeneous terrain, created from a level wooden platform (dimensions 2.4 m wide x 3.6 m long) covered by a firm rubber mat. Obstacles consisted of a single row of vertical polycarbonate posts (radius, $r = 0.023$ m) anchored to the platform (see Fig. 2). Before each experiment, the robot motor configuration was reset and the robot was manually positioned and oriented so the initial heading was transverse to the post row. Positions of infrared-reflective markers atop each robot segment were identified and recorded at 120 Hz by four Optitrack Flex13 infrared cameras (positions were accurate to within 0.1 mm). Using the tracking data, we quantified the final heading of the robot, θ (see Fig. 2b-c), for each trajectory by identifying and fitting lines to the extrema of segment trajectories (for at least three undulations) after the tail had moved beyond the post row.

2. Wheel friction

To characterize the robot-substrate interaction forces during movement, we designed a custom, 3D printed bracket to attach a single pair of Lego wheels to a 6-axis force-torque transducer (Nano 43, ATI Industrial Automation, Apex, NC, USA) and mounted the force sensor to a 6-axis industrial robot arm (Denso VS087A2-AV6-NNN-NNN). The robot arm was programmed to repeatedly execute the following automated procedure: (1) rotate the wheels by a specified angle, ψ, relative to the dragging direction and begin recording forces at 1 kH; (2) lower the wheels to a predetermined height, H, at which point wheel contact with the substrate (ethylene-vinyl acetate (EVA) Soft Linking Mats) had been established and the normal load on the wheels was comparable to the weight of a robot segment; (3) horizontally translate the wheels 40 cm across the substrate at a constant speed, $v = 10$ mm/s; (4) raise the wheels, stop recording forces, and return to the initial position.

Five trials were performed per ψ, which was varied from 0° to 90° (parallel to perpendicular to the wheel axle) in increments of one degree. For each trial, forces were decomposed into components along the wheel axle, $F_\perp$, and along the preferred rolling direction, $F_\parallel$. Force components quickly reached and subsequently maintained a near-constant value for most of the dragging distance, therefore, we estimated the steady-state values by averaging each component over the five trials within this near-constant window. Functions were fit to $F_\perp$ and $F_\parallel$ (shown as the curves in Fig. 1d) these forces could be incorporated into the Chrono simulation. Numerical values of fit parameters along with corresponding 95% confidence intervals are given in Table S1.

$$F_\perp(\psi) = a\psi + \frac{b}{1 + e^{-\psi/c}} + d$$

$$F_\parallel(\psi) = p_1\psi^4 + p_2\psi^3 + p_3\psi^2 + p_4\psi + p_5$$

3. Simulation

The simulation-based studies conducted relied on an open-source simulation framework called Chrono [1]. For a constrained multibody dynamics problem, Chrono formulates a set of index three differential-algebraic equations whose solution captures the time evolution of the dynamic system. All simulation results reported here were obtained

TABLE S1. fit parameter values and 95% confidence intervals for $F_\parallel$ and $F_\perp$.

parameter	value	95% confidence interval
a	0.0011	$(0.0010, 0.0012)$
b	0.47	$(0.42, 0.51)$
c	1.1	$(0.98, 1.21)$
d	-0.19	$(-0.24, -0.15)$
p_1	-7.8×10^{-9}	$(-1.2 \times 10^{-8}, -3.1 \times 10^{-9})$
p_2	1.2×10^{-6}	$(2.9 \times 10^{-7}, 2.1 \times 10^{-6})$
p_3	-8.7×10^{-5}	$(-1.4 \times 10^{-4}, -3.2 \times 10^{-5})$
p_4	0.0030	$(0.0018, 0.0043)$
p_5	0.097	$(0.089, 0.110)$

TABLE S2. Attributes of the snake and posts in the simulation.

Snake geometry	Segment length	5.1 cm
	Segment height	3.5 cm
	Segment width	3.2 cm
	Head radius	1.92 cm
	Tail radius	1.8 cm
	Tail height	3.5 cm
	Joint radius	1.85 cm
	Density	1.2 g/cm^3
Snake motion	Wave amplitude (ζ_{max})	0.605 rad
	Wave frequency (f)	0.15 Hz
post	Radius	2.25 cm
	Height	20 cm
	Density	1.2 g/cm^3

using a half implicit, first order, symplectic Euler time integration method and a successive over-relaxation iteration scheme. Geometric overlaps between contacting objects was used to approximate local deformations at contact points. The contact force between mating surfaces was calculated via a Hertzian contact force model [2],

$$F_n = k_n \delta_n - g_n v_n^r$$

$$F_t = k_t \delta_t,$$

where the subscripts n and t denote the contact force components, F_n and F_t, in the normal and tangential directions, respectively, δ_n is the overlap of two interacting bodies, v_n^r is the relative velocity of the bodies at the contact point, δ_t is a relative displacement in the tangential direction at the contact point, and the friction force is capped as $F_t \leq \mu F_n$ (for more detail, see [3]). For the contact of parallel cylinders, $k_n = \pi/4Y^*l$ is the contact stiffness modulus and $k_t = 2k_n/7$. Here l is the cylinder length, i.e. the height of a segment, and Y^* is the effective Young's modulus, defined based on Young's modulus, Y, and Poisson's ratio, ν, of the mating surfaces as

$$1/Y^* = (1 - \nu_1^2)/Y_1 + (1 - \nu_2^2)/Y_2.$$

Contact forces between a post and a segment with a flat surface were calculated in a similar fashion. To allow for larger integration time-steps and thus reduce simulation time, the value of Young's modulus was chosen to be smaller than the actual one. Drawing on a sensitivity analysis that quantified the impact of relaxing Y on the accuracy of the simulation results, we used $Y = 2.5 \times 10^6$ and $\nu = 0.4$. The damping coefficient, g_n, depends on the material coefficient of restitution and collision scenario [4]. We used a larger value, g_n ($\sim 10^3$), to enforce a plastic contact.

The geometry of the snake model was modeled through a set of shape primitives such as box and cylinders. The body components were connected by revolute joints, which removed five out of six relative degrees of freedom. Additional light-weight cylinders were positioned on the joints to facilitate, from a geometric perspective, a smooth interaction of the segments with the cylindrical posts. Table S2 shows parameter values used.

Simulations were then validated by comparing experimental and simulated trajectories and forces for snake interacting with a single post. In experiments, forces exerted by the robot during collisions with the post were recorded by mounting the post to an ATI Nano 43 6-axis force-torque transducer. Forces exerted by the robot onto the posts for the trials shown in Fig. 2 are shown in Fig. S1a (single post) and Fig. S1b (multi-post). This comparison is representative of agreement between simulation and experiment: trajectories for similar collision states produced nearly-identical trajectories and forces were often comparable and exhibited similar structure in both simulation and experiment. While there were some quantitative differences between simulation and experimental forces, these discrepancies did not seem to affect the kinematic agreement. A time step convergence analysis revealed that forces and resulting trajectories were insensitive to the time step, Δt, for $\Delta t < 6 \times 10^{-4}$ s. $\Delta t = 10^{-4}$ s was selected for all the simulations presented here.

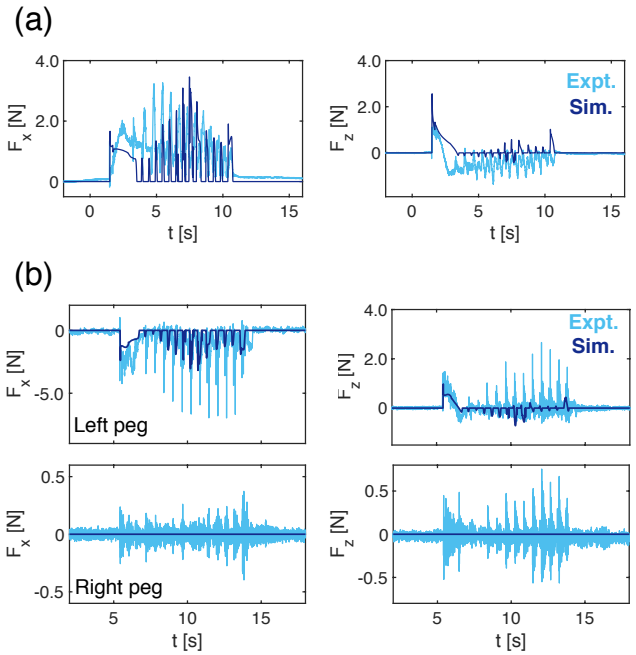

FIG. S1. **Experimental and simulation forces on posts.** (a) Forces exerted onto the post by the robot during the trajectory shown in Fig. 2b. (b) Forces exerted onto the posts by the robot during the trajectory shown in Fig. 2c.

In the multi-post simulations, the accuracy of the results improved significantly when, to mirror the presence of the revolute joints in the physical prototype, the snake model was augmented with spheres connecting the boxes used for the snake segments. The diameter of the connecting spheres was identical to the width of the robotic snake. The width of the cubic segments in the simulation was slightly reduced from that of the robotic snake to bury the edges inside the spherical joints and prevent the edge contact, particularly at large time step. Table S2 summarizes the attributes of the snake and the posts for simulations presented here.

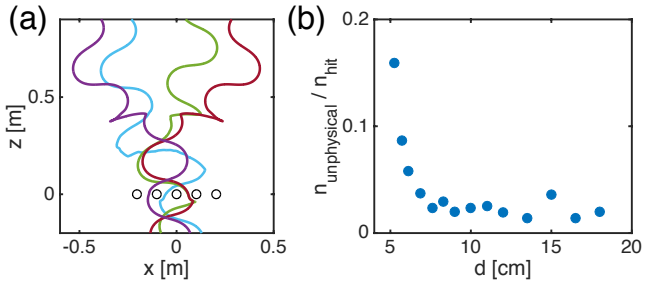

FIG. S2. **Unphysical simulation trajectories.** (a) Four examples of unphysical trajectories for $d = 5.7$ cm. The robot becomes pinned after the head has cleared the posts, and as a result, the body is rapidly reoriented. These situations do not occur in the experiment. (b) Fraction of simulations for each spacing that are unphysical.

At least 1,000 simulations were run for each post configuration, and for each configuration, there were a few trajectories which were not physical. These typically occurred when the tail of the snake became stuck on the post, causing the entire snake to rapidly change direction. Four representative examples are shown in Fig. S2a. These were identified and removed from further analysis using the following criteria: if, at any point after the head has moved beyond the post row, (1) velocity of head is at least twice as large as maximum head velocity for the freely-moving snake, $v_{head} \geq 2v_{max,free}$ and (2) force on the head does not exceed a nominal value, chosen here to be $F_{head} \leq 0.01$ N. Fig. S2b shows (for $\zeta_{max} = 0.605$ rad), as a function of post spacing, how many unphysical trajectories occurred relative to the number of simulations that had collisions with the posts.

4. Small and large ζ_{max}: Qualitatively different spacing dependence

We find that the distribution dependence on spacing presented in Fig. 10 does not hold for all ζ_{max} angular amplitudes of oscillation. If ζ_{max} is sufficiently small, the distance swept out in a single cycle, $2\ell\zeta_{max}$ does not exceed the post diameter, $2r$. The qualitative behavior change we observe for small ζ_{max} is consistent with this observation, falling to the left of the dashed line in Fig. 10c. For large ζ_{max}, the body becomes very curved and points along the body in the direction of travel are no longer monotonically increasing from tail to head. We suspect that this may set a qualitative change in behavior as well. Fig. S3 shows the dependence of the spread of the distributions, θ_{70}, on the inter-post spacing, d, for two amplitudes with qualitatively different behavior.

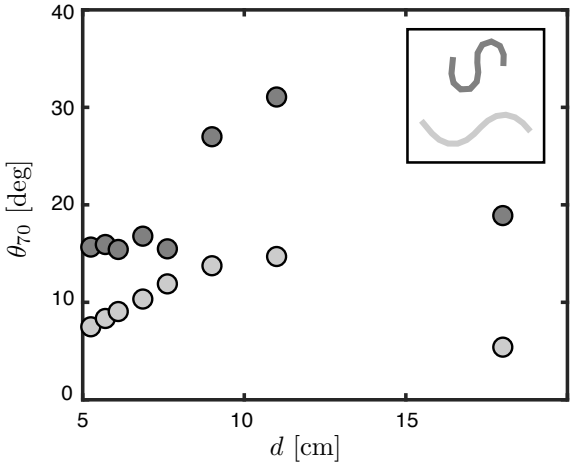

FIG. S3. **Scattering angle distribution dependence on spacing for large and small angular amplitude.** When ζ_{max} is outside of the range presented in the main text, the qualitative dependence of θ_{70} on d changes. The light gray points show this dependence for small ζ_{max}, and the dark gray points show the dependence for large ζ_{max}

5. Multi-post configuration: One dominant head collision

To demonstrate that there is one dominant collision in the multi-post configuration, we first show that most simulations, even for small spacings, had one head-post collision. Fig. S4a shows how many of the simulations, n_{hit}, had at least one collision between the head of the snake and the post row relative to the total number of simulations, n_{sim}. The number of simulations in which two or more collisions occurred, n_{2+}, compared to n_{hit} is shown in Fig. S4b.

Of the simulations in which multiple collisions occur, we next show that the second-longest collision is typically not of comparable duration. In Fig. S4c, two-dimensional probability densities of second-longest vs longest duration are shown for four post configurations. If collisions were of comparable durations, the density of points would lie along the black lines in each plot. However, in each case, most of the points are concentrated below the line. This, along with the decreasing number of simulations for which multiple collisions occur, confirms that there is typically one dominant collision.

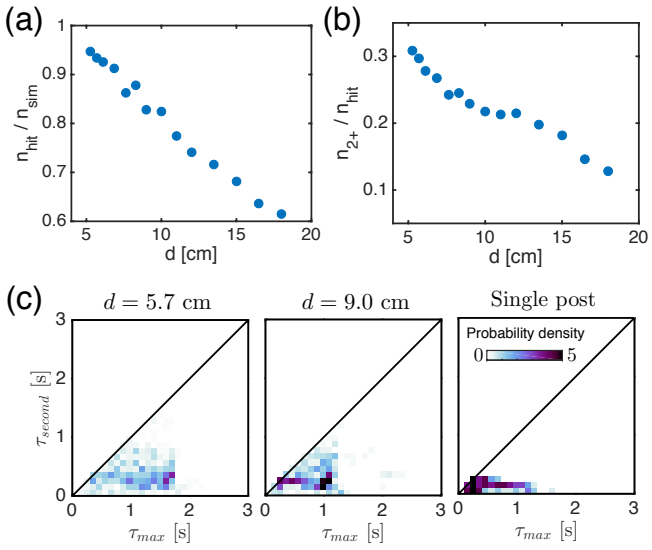

FIG. S4. **Fraction of simulations with head collisions.** (a) Fraction of simulations for which at least one head-post collision occurred as a function of spacing. (b) Fraction of simulations in (a) for which two or more collisions occurred. (c) Probability maps for second-longest vs longest durations for $d = 5.7$ cm (left) to $d = 9.0$ cm (middle) to single post (right). Only simulations for which there were at least two collisions are shown here.

6. Single- and multi-post collision states

Fig. S5 shows how the density collision states depends on the inter-post spacing. For the single-post simulations (bottom right), all allowed states are evenly-sampled. As spacing is decreased, certain undulation-phase and impact location collision states become inaccessible, and others become more likely to occur. These excluded regions become larger as spacing becomes smaller, and the non-uniformity of the densities of remaining states becomes more pronounced.

For each post configuration, initial conditions within the relevant region were randomly generated. Therefore, we did not necessarily have information about precisely the same collision for single- and multi-post configurations. Therefore, to determine how collision states were influenced by the presence and location of additional posts, we identified, in (η, ϕ) space, the single-post state closest to each multi-post state by minimizing $\delta_{\eta\phi} = \sqrt{(\eta_s - \eta_m)^2 + (\phi_s - \phi_m)^2}$.

The distributions of distances between the single- and multi-post states are shown in the left column of Fig. S6. These distributions do not depend on post spacing, and in all cases, distances are typically small, so single-post points assigned to multi-post states are nearby in (η, ϕ) space. As a final check, we show in the right column of Fig. S6 that there is no significant correlation between $\delta_{\eta\phi}$ and deviation from the $\omega\tau_m = \omega\tau_s$ trend. Two-dimensional PDFs for two post configurations are shown, and the corresponding correlation coefficient for each spacing is given in each plot.

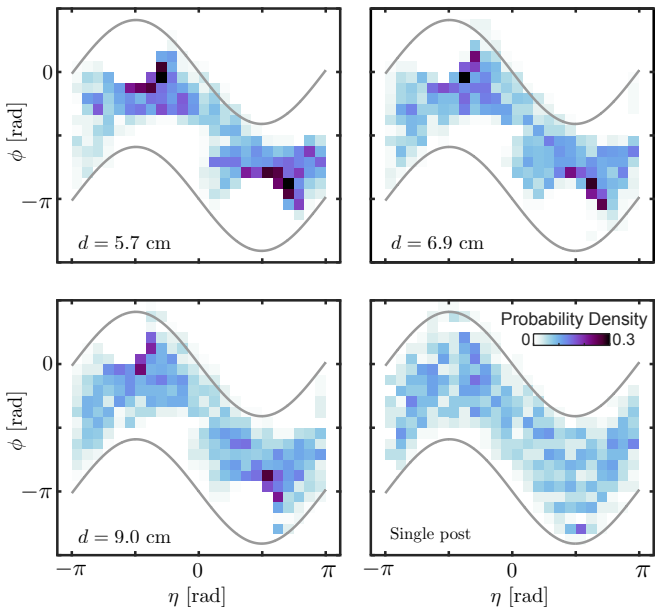

FIG. S5. **Densities of collision states.** Densities of states in the space of impact locations, ϕ, and wave phases, η. These states are shifted around as spacing is changed. In the single-post case, all allowed states are evenly sampled. As spacing is decreased when multiple posts are present, some regions become inaccessible and others more favored.

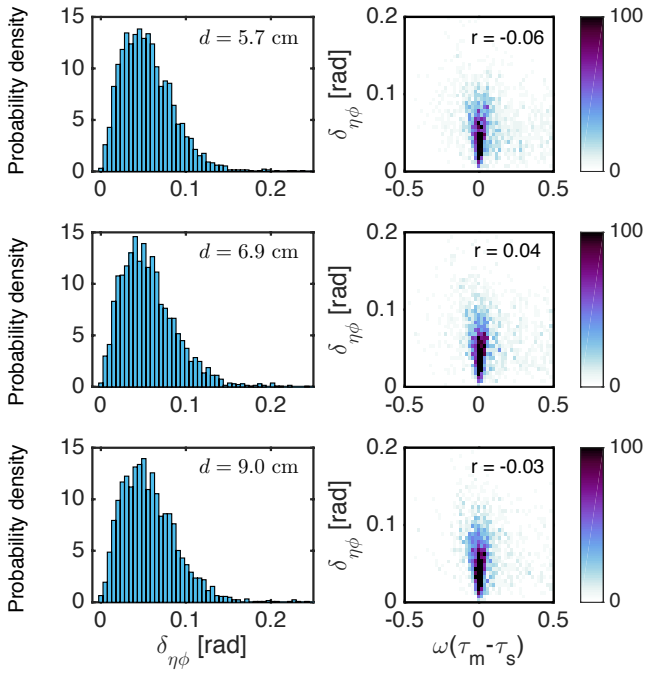

FIG. S6. **Distances between single- and multi-post states.** Each row shows data for a spacing specified in left plot. Left column: Probability distributions of distances between nearest single and multi-peg states (nearest is defined by the smallest euclidean distance between states in (η, ϕ)-space). Right column: Two dimensional PDFs showing that there is no significant correlation between deviation from $\omega\tau_m = \omega\tau_s$ line and distance between nearest single- and multi-peg collision states.

7. Supplementary movies

Movie 1. **Robotic snake in single-post environment.** A view of the robotic snake moving toward and interacting with a single post. The sliding/pushing head-post interaction is visible here.

Movie 2. **Robotic snake in multi-post environment.** An overhead view of several experiments in which the robotic snake moving toward, interacting with, and subsequently exiting the multi-post array (here, $d = 5.7$ cm). The final heading depends on the initial placement of robot, which is varied along the fore-aft direction here.

Movie 3. **Simulated snake in multi-post environment.** Three examples of the simulated snake interacting with a multi-post array ($d = 5.7$ cm).

Movie 4. **Emergence of preferred directions.** Summation of binary images created from the head trajectory of the robot in each of 329 experiments for $d = 5.7$ cm. Trajectories from different initial positions are added in a randomized order. As more experiments are included, a more complete picture of possible interactions and outcomes appears and preferred scattering directions emerge.

[1] A. Tasora, R. Serban, H. Mazhar, A. Pazouki, D. Melanz, J. Fleischmann, M. Taylor, H. Sugiyama, and D. Negrut, in *High Performance Computing in Science and Engineering Lecture Notes in Computer Science*, edited by T. Kozubek (Springer, 2016) pp. 19–49.
[2] K. L. Johnson, *Contact mechanics* (Cambridge University Press, 1987).
[3] J. Fleischmann, R. Serban, D. Negrut, and P. Jayakumar, Journal of Computational and Nonlinear Dynamics **11**, 044502 (2016).
[4] M. Machado, P. Moreira, P. Flores, and H. M. Lankarani, Mechanism and Machine Theory **53**, 99 (2012).